PHYSICAL REVIEW B **92**, 201202(R) (2015)

Ultrahigh exciton diffusion in intrinsic diamond

Hikaru Morimoto,[1] Yuji Hazama,[1,*] Koichiro Tanaka,[1,2,3] and Nobuko Naka[1,†]

[1]*Department of Physics, Kyoto University, Kitashirakawa-Oiwake-cho, Sakyo-ku, Kyoto 606-8502, Japan*

[2]*Institute for Integrated Cell-Material Sciences (WPI-iCeMS), Kyoto University, Kyoto 606-8501, Japan*

[3]*Core Research for Evolutional Science and Technology (CREST), JST, Kyoto 606-8502, Japan*

(Received 24 May 2015; revised manuscript received 12 October 2015; published 16 November 2015)

We observe exceptionally high diffusion of excitons in diamond using time-resolved photoluminescence imaging. The diffusivity is found to increase with decreasing temperature more rapidly than well-established predictions. The highest diffusion constant, 9.2×10^3 cm^2/s, measured for thermalized excitons is 150 times that recorded previously in diamond. We elucidate the momentum relaxation mechanisms determining transport: intraband and interband scattering by acoustic phonons in the exciton fine-structure levels. The enhanced diffusivity above 100 K is explained by a free-carrier contribution.

DOI: 10.1103/PhysRevB.92.201202 PACS number(s): 71.35.−y, 63.20.kk, 72.10.Di, 78.47.D−

The *intrinsic* diffusivity of carriers is a key parameter for determining their transport properties. A high diffusivity is associated with high mobility via the Einstein relationship and leads to preferable device characteristics, such as high operation speed and low-energy consumption [1]. The topic of carrier diffusivity is also relevant to new physics because the temperature dependence of diffusivity reveals the mechanisms of carrier momentum relaxation due to scattering by phonons, impurities, or other carriers. The investigation of carrier scattering processes using terahertz time-domain spectroscopy [2], angle-resolved photoemission spectroscopy [3], and quantum Hall effect measurements [4], along with full first-principles calculations [5], is an emerging field.

Among the major high-mobility materials, such as Si, Ge, GaAs, and GaN, diamond is an indirect-type semiconductor with the widest band gap (5.49 eV). Diamond has been attracting rapidly increasing attention for use in power electronics, spintronics, quantum optics, and nuclear physics experiments. All these applications are made possible by the mobility in intrinsic diamond. Currently, the impurity-vacancy centers, which function as spin qubits or single-photon emitters [6], are embedded in intrinsic diamond layers, and the mobility is particularly crucial when the centers are electrically driven. Not only free carriers but also excitons—electron-hole pairs bound by the Coulomb force—could play essential roles in mobility because the large exciton binding energy of 80 meV causes an exceptional situation in which the excitons are stable up to room temperature. Owing to chemical equilibration between free carriers and excitons having different effective masses, charge carrier mobility is affected by exciton mobility and vice versa. In diamond-based light-emitting diodes (LEDs) or electron emitters, excitons are formed in the intrinsic active layer even under current injection, dominating ultraviolet emission [7] or providing efficient photoelectron production [8]. The emission efficiency of ultraviolet LEDs is actually improved by redesigning the intrinsic layer thickness assuming higher exciton diffusivity [7]. In diamond irradiated by high-energy particles [9,10] or synchrotron radiation [11], electron-hole pairs are produced, and the particles/radiation can be detected by charge collection at electrodes, the efficiency of which is determined by the charge transport over macroscopic distances [12]. The role of exciton formation in such diamond detectors seems to be unexplored, despite its use in cryogenic conditions [13] and under an electric field (<10 kV/cm) well below the tunnel ionization threshold (∼600 kV/cm) for excitons.

For more practical and efficient uses of these devices, it is inevitable that the fundamental physics behind them is elucidated. This can be achieved by determining the diffusivity of intrinsic diamond across a wide temperature range. However, mobility measurements in diamond have long been limited to above 80 K [14–17] because carrier freezing at deep impurity levels hinders electrical transport measurements. Recent attempts to measure the mobility at lower temperatures utilized photoexcited charge carriers in undoped diamond [18,19] through light-induced transient grating [20–22], time-resolved photoluminescence (PL) [22], cyclotron resonance [23], and excitons through cathodoluminescence [24]. Unfortunately, the reported mobility values have varied significantly because most of them were reduced due to *extrinsic* factors, such as band-gap renormalization [20], the thermal grating effect [22], and carrier heating by Auger recombination [22] that occurs at high carrier densities (∼10^{20} cm^{-3}) [25].

In this Rapid Communication, we directly obtain snapshots of spatial exciton expansion in ultrapure diamond through time-resolved PL imaging. We temporally separate the transport properties of the high- and low-injection regimes and extract the *intrinsic* diffusivity of thermally equilibrated excitons. At cryogenic temperatures, the measured diffusivity significantly exceeds the predictions based on the previously established $T^{-1/2}$ temperature dependence for acoustic-phonon scattering. Consequently, the diffusion constant measured at 2 K, 9.2×10^3 cm^2/s, is found to be exceptionally high among high-purity traditional semiconductors (Si, Ge, GaAs, and Cu_2O). We also identify the exciton transport mechanisms and evaluate the exciton/free-carrier contributions up to room temperature.

Before describing the experimental results, we briefly review the indirect excitons in diamond. They are formed at the Δ points, about 76% of the zone boundaries along the [100] axes in wave-vector (k) space, where the sixfold minima

*Present address: The Institute for Solid State Physics, The University of Tokyo, Kashiwanoha, Kashiwa, Chiba 277-8581, Japan.
†naka@scphys.kyoto-u.ac.jp

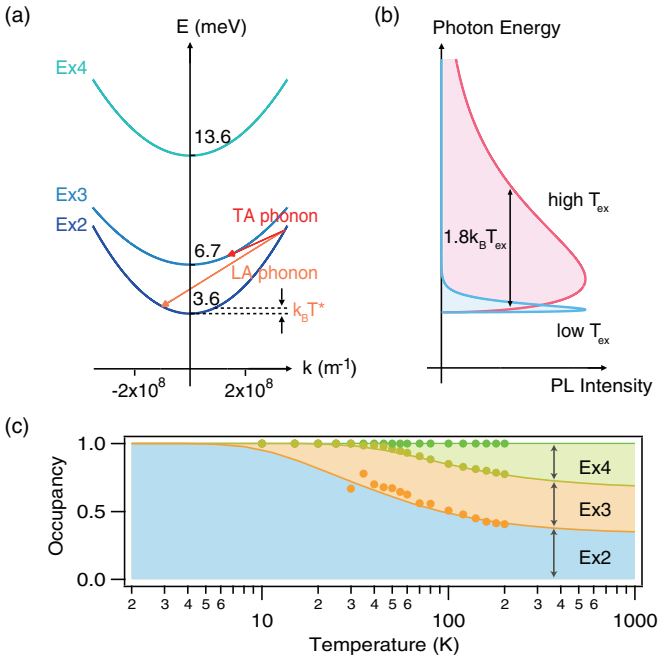

FIG. 1. (Color online) Schematic of (a) exciton energy dispersion and relaxation by phonon emission, and (b) PL line shapes for different exciton effective temperatures T_{ex}. T^* indicates the characteristic temperature for longitudinal acoustic phonons. Exciton masses $m_2 = 0.65m_0$, $m_3 = 1.05m_0$, and $m_4 = 0.76m_0$ [27], where m_0 is the free-electron mass, are used. (c) Occupancy of the fine-structure levels. The dots were derived from the spectral weights, and solid lines represent $f_i = \exp(-\Delta E_i/k_BT)$ normalized to the sum $\sum_{i=2,3,4} f_i$, where $\Delta E_2 = 3.6$ meV, $\Delta E_3 = 6.7$ meV, and $\Delta E_4 = 13.6$ meV [26].

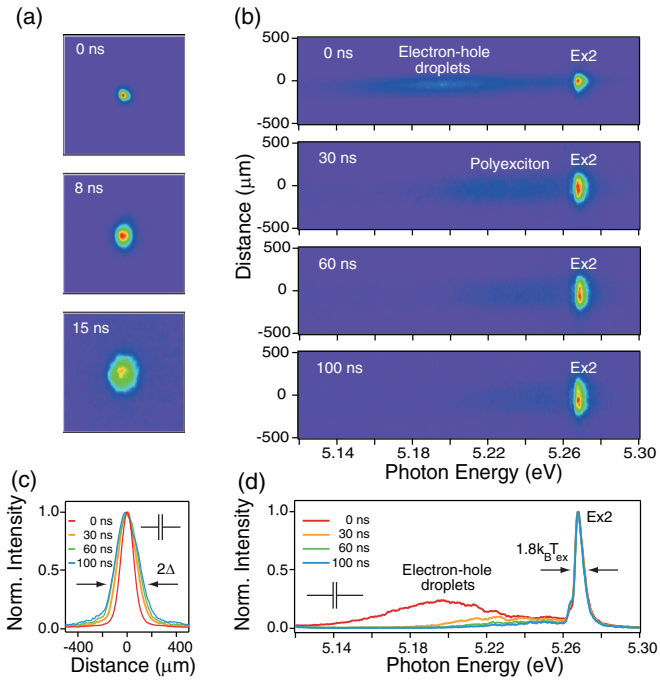

FIG. 2. (Color online) (a) Time-resolved PL image obtained at 7 K for different delay times: 0, 8, and 15 ns. The gate width was 1 ns. The area of each image is 1.0×1.0 mm^2. (b) Spectrally resolved PL image at 20 K for 0, 30, 60, and 100 ns. The gate width was 10 ns. (c) Vertical profiles of the images at 20 K. (d) Time-resolved PL spectra at 20 K, normalized at Ex2.

of the conduction band are located. The long controversy regarding the exciton fine structure has recently been resolved by the inclusion of effective-mass anisotropy [26]. Among 12 fine-structure states, four sublevels appear in PL, with the one at the lowest energy (Ex1) being a nearly dark state. The upper three exciton sublevels (Ex2–Ex4) are derived from the optically active states. The exciton energy dispersion $E = \Delta E_i + \hbar^2k^2/(2m_i^*)$ is depicted in Fig. 1(a), together with the phonon dispersion, where ΔE_i $(i = 2,3,4)$ is the fine-structure splitting energy measured from the Ex1 level, $\hbar$ is the reduced Planck constant, and we used a different translational mass m_i^* [27] for each exciton band. Excitons relax with phonon emission and absorption within/between these exciton bands, which leads to their diffusion. The Ex1 band is omitted in Fig. 1(a) because we neglected the scattering of bright excitons (Ex2, Ex3, and Ex4) into Ex1, which is considered a spin-forbidden process.

The PL originating from indirect excitons occurs with the assistance of phonon emission by satisfying the conservation of energy and momentum during the optical transition. As the spectral shape [28] reflects the energy distribution of excitons in the band [Fig. 1(b)], the effective temperature T_{ex} of the carrier system is obtained from the PL spectral width. We note that T_{ex} generally can be higher than the lattice temperature. In addition, the occupancy f_i of excitons in each sublevel can be determined based on the spectral weights of the fine-structure peaks in PL [26]. The results are shown in Fig. 1(c), indicating that occupancies of the two higher levels dominate over that in Ex2 above 100 K.

We used a chemical-vapor-deposition diamond (Element Six Ltd.) with the unintentionally incorporated dopants of less than 5 ppb of nitrogen and 1 ppb of boron. We created excitons at a density around 10^{17} cm^{-3} by using photoabsorption at 5.51 eV, with the 2.5 ns pulses from an optical parametric oscillator (Ekspla, NT242-2). This unique excitation method minimizes the heating of the lattice during the photoexcitation process [29], and enables efficient thermalization of excitons. The time-resolved spatial image of the exciton PL was dispersed by a monochromator (Horiba Jobin Yvon, iHR550) and detected by a gated CCD camera (LaVision, Picostar HR).

Figure 2(a) shows the spatial distribution of the PL intensity at different delay times for diamond kept at 7 K in a cryostat. The initial spot size was 38.3×39.5 μm^2. With increasing delay time following the photoexcitation at $t = 0$, the exciton cloud expanded laterally by about 300 μm within 15 ns, implying a vast diffusivity. Figure 2(b) shows spectrally resolved images taken at 20 K. The ordinate retains the spatial information whereas the abscissa indicates the photon energy. The recombination of excitons (Ex2) is seen at around 5.26 eV. The intensity of Ex1 is very weak because the optical transition is nearly forbidden [26]. The occupancies of the higher sublevels, f_3 and f_4, are nearly zero because of the low lattice temperature [see Fig. 1(c)]. The broad feature at lower photon energies is due to electron-hole droplets for a delay time of 0 ns and to polyexcitons [30] at later delay times. Figure 2(c) shows the temporal evolution of the spatial profile.

The spectrally resolved PL intensity was integrated over the exciton fine-structure peaks. The profiles can be approximated by a Gaussian line shape, and the half width Δ was obtained by the fit. Figure 2(d) shows time-resolved PL spectra. Based on the spectral analysis, we confirmed that the excitons reach internal thermal equilibrium [31–33] during photoexcitation and that the relaxation time for the excitons to equilibrate with the lattice is shorter than 100 ns [34].

In order to extract the diffusion constant D, we assumed a two-dimensional expansion of the exciton cloud. The effects of surface recombination [22] and diffusion into the sample depth were negligible because we choose bulk excitation with more than 30% transmission of the incident light through a sample of 0.5 mm thickness [29]. Two-dimensional diffusion is described by the equation

$$\frac{\partial n}{\partial t} = D\left(\frac{\partial^2}{\partial x^2} + \frac{\partial^2}{\partial y^2}\right)n - \frac{n}{\tau}, \tag{1}$$

where n is the exciton density and τ is the exciton lifetime in the range of hundreds of nanoseconds at 7–300 K [35]. The solution, assuming an initial Gaussian distribution with a half width d at time $t = t_0$, is given by

$$n(x,y,t) = \frac{n_0}{1 + 8D(t - t_0)/d^2} \times \exp\left[-\frac{2(x^2 + y^2)}{d^2 + 8D(t - t_0)} - \frac{(t - t_0)}{\tau}\right]. \tag{2}$$

The squared width of the cloud at time t is given by the relation

$$\Delta^2(t) = d^2/2 + 4D(t - t_0), \tag{3}$$

which indicates a linear dependence on time.

Figure 3 plots Δ^2 as a function of t. The squared widths show a nearly linear time dependence above 100 K, and D was obtained by the fit with Eq. (3), as indicated by the solid lines in Fig. 3(a). On the other hand, the expansion at low temperatures exhibits a sublinear dependence, as in Fig. 3(b). We interpreted this result as an indication that the expansion is caused by two different origins which are temporally separable. The early component for the time window 0–20 ns has a correlation with the appearance of electron-hole droplets in the PL, and is apparently due to their fast expansion driven by the phonon wind [36]. Considering this time scale and the relaxation time, we extracted the diffusion constants of the later expansion by setting $t_0 = 100$ ns and $d = \sqrt{2}\Delta(t_0)$ in Eq (3). The fitting curves are shown by the solid lines.

The temporal change at 2 K was distinctive because of the superlinear behavior in diffusion. The expansion in the absence of electron-hole droplets at low injection is shown in the inset of Fig. 3(b). Since D varied with delay time according to the gradual change of the effective temperature during the 12-ns lifetime, we used the relation $\Delta^2(t_1) - \Delta^2(t_2) = 4D(t_1 - t_2)$. The diffusion constant for $t_1(t_2) = 0(8)$ ns is $D = 4.5 \times 10^3$ cm^2/s, whereas that for $t_1(t_2) = 9(14)$ ns is even higher, $D = 9.2 \times 10^3$ cm^2/s, corresponding to an exciton mobility as high as 3×10^7 cm^2/(V s). The effective temperatures derived from the spectral analysis, 5.5 and 4.0 K, are used in the subsequent plot.

The extracted diffusion constants up to 300 K are summarized in Fig. 4, showing that the diffusion constant tends

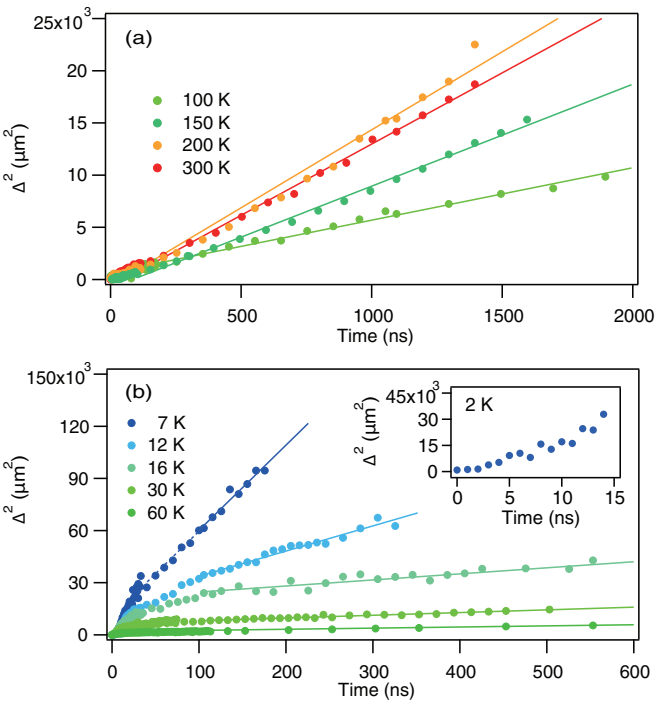

FIG. 3. (Color online) Plots of Δ^2 as a function of delay time for temperatures (a) above 100 K and (b) below 60 K. The initial width at $t = 0$ has been subtracted. A detection window corresponding to (a) 60 μm or (b) 1800 μm width on the sample was used.

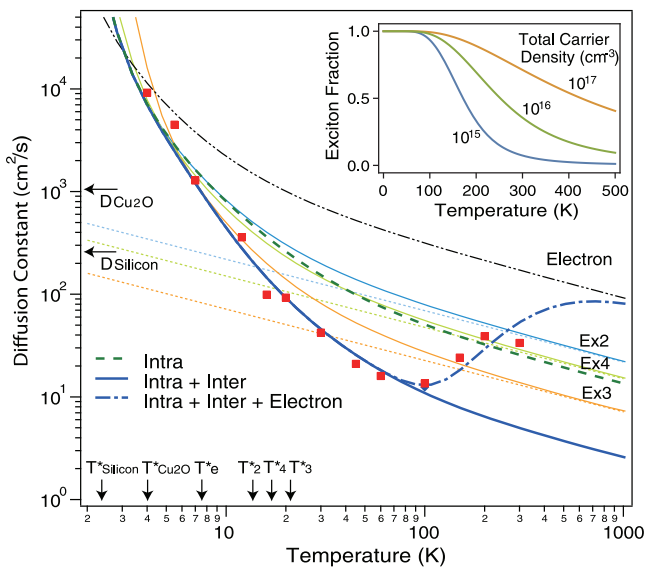

FIG. 4. (Color online) Measured diffusion constants (squares) in comparison with the calculated ones. The dashed double-dotted line and thin solid lines represent intraband scattering of electrons [23] and excitons, respectively. The dashed and thick solid lines indicate weighted averages for the intraband and the intraband plus interband, respectively. The dashed-dotted line includes exciton ionization assuming a total carrier density $n_t = 1.0 \times 10^{17}$ cm^{-3}. The inset shows a fraction of excitons to $n_t = 10^{15\text{–}17}$ cm^{-3}, calculated according to the mass-action law with an equilibrium constant of 1.2×10^{16} cm^{-3} at 300 K [41].

to increase with decreasing temperature. The low-temperature values we observed are higher by two orders of magnitude than the diffusivity previously reported for thermalized excitons, 60 cm^2/s [37]. The diffusion constant slightly increases on the high-temperature side, and the values above 100 K are in reasonable agreement with those previously reported [21,22].

In order to understand the temperature dependence, we numerically calculate the momentum relaxation time τ_p of exciton intraband scattering from longitudinal acoustic phonons ($v_l = 17.5$ km/s [38]). We assumed an inelastic deformation potential interaction [39] with a strength of 10 eV, which is the value for holes [23], since the deformation potential for excitons is unknown. The thin solid lines in Fig. 4 are the calculated diffusion constants $D_i = ek_BT\langle\tau_p\rangle/m_i^*$, which clearly exceed the classical predictions from the $T^{-1/2}$ relation (the dotted lines). Here, the angle brackets indicate the average over the thermal distribution, and e and k_B represent the elementary charge and Boltzmann constant, respectively. The occurrence of the low-temperature anomaly is related to the characteristic temperature defined as $T_i^* = m_i^* v_l^2/k_B$ [40], below which the phonon emission process freezes out due to the lack of a final state that conserves energy and momentum [see Fig. 1(a)]. The slightly different T_i^*'s for the different exciton species are shown near the horizontal axis of Fig. 4. Since the measured temperature dependence is apparently more rapid, we further include the exciton interband scattering due to transverse acoustic phonons ($v_t = 12.8$ km/s [38]). The weighted average of the diffusion constant $D_{\rm net} = \sum_{i=2,3,4} m_i^{*3/2} f_i D_i / \sum_{i=2,3,4} m_i^{*3/2} f_i$ is shown by the thick solid line, where the Boltzmann distribution $f_i = \exp(-\Delta E_i/k_BT)$ as shown in Fig. 1(c) is assumed for the level occupancy. The calculation reproduces the diffusivity measured below 100 K much better than the weighted average without interband scattering (the dashed line).

As proposed in recent reports [21], we attribute the increased diffusivity above 100 K to be due to ionized excitons, namely, unbound charge carriers in chemical equilibrium with the exciton system. The inset of Fig. 4 shows a fraction of excitons to the total number of excitons and free carriers, calculated by assuming the mass-action law [41]. The diffusivity including the contribution from the free electrons is shown by the dashed-dotted line. The excellent agreement of the calculations with the data across the whole temperature range confirms that exciton transport in diamond is determined by multiple mechanisms: intraband and interband scattering by acoustic phonons in the exciton fine-structure levels and exciton ionization into free carriers. The last process implies that the contribution of excitons becomes more dominant at higher injections (see the inset), which might affect device performance via the reduction in charge carrier mobility due to coexisting excitons with heavier translational masses.

Finally, we would like to emphasize the uniqueness of our measurements. The breakdown of the $T^{-1/2}$ relation, which leads to higher mobilities due to the suppressed phonon emission, was predicted decades ago [42]. This low-temperature anomaly, however, was observed only in Cu_2O below 6 K [40] because it is usually obscured by impurity scattering and unwanted carrier heating. Our success in diamond relies on the relatively high T^* originating from the high sound velocity [38] and large effective masses [27], the high purity of our sample, and, most importantly, our deliberated procedure for generating cold excitons [29]. Owing to the cooling of the excitons from 20 to 4 K, the diffusivity was drastically enhanced. The exceptionally high diffusion constant, 9.2×10^3 cm^2/s, for thermalized excitons is 150 times that reported previously, more than 30 times that of high-purity silicon at 1.3 K [43], and approximately nine times greater than that of Cu_2O at 1.2 K [40].

In summary, we measured the exciton diffusion in ultrapure diamond by time-resolved PL imaging. The measured diffusivity in diamond at 2 K was exceptionally high among semiconducting materials. After clarifying the transport mechanisms of excitons and the low-temperature regime of acoustic-phonon scattering, we successfully separated the free-carrier contribution to the exciton diffusion above 100 K. Our results lay the basis for an improved understanding of the deformation potential interaction, and will motivate general interest in intrinsic scattering mechanisms that set a mobility limit in various materials ranging from traditional semiconductors, and carbon allotropes (graphite, graphene, carbon nanotubes) to organic molecular conductors.

This work was partially supported by Grant-in-Aid for Scientific Research from JSPS (Grants No. 26400317 and No. 15K05129).

[1] A. Hiraiwa and H. Kawarada, Figure of merit of diamond power devices based on accurately estimated impact ionization processes, J. Appl. Phys. **114**, 034506 (2013).

[2] E. Hendry, M. Koeberg, J. Pijpers, and M. Bonn, Reduction of carrier mobility in semiconductors caused by charge-charge interactions, Phys. Rev. B **75**, 233202 (2007).

[3] T. Ichibayashi and K. Tanimura, Ultrafast Carrier Relaxation in Si Studied by Time-Resolved Two-Photon Photoemission Spectroscopy: Intravalley Scattering and Energy Relaxation of Hot Electrons, Phys. Rev. Lett. **102**, 087403 (2009).

[4] S. Engels, B. Terres, A. Epping, T. Khodkov, K. Watanabe, T. Taniguchi, and B. Beschoten, and C. Stampfer, Limitations to Carrier Mobility and Phase-Coherent Transport in Bilayer Graphene, Phys. Rev. Lett. **113**, 126801 (2014).

[5] O. D. Restrepo, K. Varga, and S. T. Pantelides, First-principles calculations of electron mobilities in silicon: Phonon and Coulomb scattering, Appl. Phys. Lett. **94**, 212103 (2009).

[6] I. Aharonovich and E. Neu, Diamond nanophotonics, Adv. Opt. Mater. **2**, 911 (2014).

[7] T. Makino, K. Yoshino, N. Sakai, K. Uchida, S. Koizumi, H. Kato, D. Takeuchi, M. Ogura, K. Ohyama, T. Matsumoto, H. Okushi, and S. Yamasaki, Enhancement in emission efficiency of diamond deep-ultraviolet light emitting diode, Appl. Phys. Lett. **99**, 061110 (2011).

[8] J. Ristein, W. Stein, and L. Ley, Defect Spectroscopy and Determination of the Electron Diffusion Length in Single Crystal Diamond by Total Photoelectron Yield Spectroscopy, Phys. Rev. Lett. **78**, 1803 (1997).

[9] M. Tsubota, J. H. Kaneko, D. Miyazaki, T. Shimaoka, K. Ueno, T. Tadokoro, A. Chayahara, H. Watanabe, Y. Kato, S. Shikata, and H. Kuwabara, High-temperature characteristics of charge collection efficiency using single CVD diamond detectors, Nucl. Instrum. Methods A **789**, 50 (2015).

[10] W. Kada, N. Iwamoto, T. Satoh, S. Onoda, V. Grilj, N. Skukan, M. Koka, T. Ohshima, M. Jaksic, and T. Kamiya, Continuous observation of polarization effects in thin SC-CVD diamond detector designed for heavy ion microbeam measurement, Nucl. Instrum. Methods B **331**, 113 (2014).

[11] D. R. Kania, M. I. Landstrass, M. A. Plano, L. S. Pan, and S. Han, Diamond radiation detectors, Diamond Relat. Mater. **2**, 1012 (1993).

[12] D. Asner *et al.*, Diamond pixel modules, Nucl. Instrum. Methods A **636**, S125 (2011).

[13] C. Kurfurst, B. Dehning, M. Sapinski, M. R. Bartosik, T. Eisel, C. Fabjan, C. A. Rementeria, E. Griesmayer, V. Eremin, E. Verbitskaya, A. Zabrodskii, N. Fadeeva, Y. Tuboltsev, I. Eremin, N. Egorov, J. Harkonen, P. Luukka, and E. Tuominen, *In situ* radiation test of silicon and diamond detectors operating in superfluid helium and developed for beam loss monitoring, Nucl. Instrum. Methods A **782**, 149 (2015).

[14] P. J. Dean, E. C. Lightowlers, and D. R. Wight, Intrinsic and extrinsic recombination radiation from natural and synthetic aluminum-doped diamond, Phys. Rev. **140**, A352 (1965).

[15] J. Isberg, J. Hammersberg, E. Johansson, T. Wilstrom, D. J. Twitchen, A. J. Whitehead, S. E. Coe, and G. A. Scarsbrook, High carrier mobility in single-crystal plasma-deposited diamond, Science **297**, 1670 (2002).

[16] J. Pernot, P. N. Volpe, F. Omnes, P. Muret, V. Mortet, K. Haenen, and T. Teraji, Hall hole mobility in boron-doped homoepitaxial diamond, Phys. Rev. B **81**, 205203 (2010).

[17] M. Gabrysch, S. Majdi, D. J. Twitchen, and J. Isberg, Electron and hole drift velocity in chemical vapor deposition diamond, J. Appl. Phys. **109**, 063719 (2011).

[18] S. Majdi, K. K. Kovi, J. Hammersberg, and J. Isberg, Hole transport in single crystal synthetic diamond at low temperatures, Appl. Phys. Lett. **102**, 152113 (2013).

[19] H. Jansen, D. Dobos, T. Eisel, H. Pernegger, V. Eremin, and N. Wermes, Temperature dependence of charge carrier mobility in single-crystal chemical vapour deposition diamond, J. Appl. Phys. **113**, 173706 (2013).

[20] P. Scajev, V. Gudelis, A. Tallaire, J. Barjon, and K. Jarasiunas, Injection and temperature dependent carrier recombination rate and diffusion length in freestanding CVD diamond, Phys. Status Solidi A **210**, 2016 (2013).

[21] P. Scajev, J. Jurkevicius, J. Mickevicius, K. Jarasiunas, and H. Kato, Features of free carrier and exciton recombination, diffusion, and photoluminescence in undoped and phosphorus-doped diamond layers, Diamond Relat. Mater. **57**, 9 (2015).

[22] M. Kozak, F. Trojanek, and P. Maly, Optical study of carrier diffusion and recombination in CVD diamond, Phys. Status Solidi A **210**, 2008 (2013).

[23] I. Akimoto, Y. Handa, K. Fukai, and N. Naka, High carrier mobility in ultrapure diamond measured by time-resolved cyclotron resonance, Appl. Phys. Lett. **105**, 032102 (2014).

[24] J. Barjon, F. Jomard, A. Tallaire, J. Achard, and F. Silva, Determination of exciton diffusion lengths in isotopically engineered diamond junctions, Appl. Phys. Lett. **100**, 122107 (2012).

[25] R. Shimano, M. Nagai, K. Horiuch, and M. Kuwata-Gonokami, Formation of a High T_c Electron-Hole Liquid in Diamond, Phys. Rev. Lett. **88**, 057404 (2002).

[26] Y. Hazama, N. Naka, and H. Stolz, Mass-anisotropy splitting of indirect excitons in diamond, Phys. Rev. B **90**, 045209 (2014).

[27] N. Naka, K. Fukai, Y. Handa, and I. Akimoto, Direct measurement via cyclotron resonance of the carrier effective masses in pristine diamond, Phys. Rev. B **88**, 035205 (2013).

[28] S. J. Sharp, A. T. Collins, G. Davies, and G. S. Joyce, Higher resolution studies of shallow bound exciton luminescence in diamond, J. Phys.: Condens. Matter **9**, L451 (1997).

[29] Y. Hazama, N. Naka, M. Kuwata-Gonokami, and K. Tanaka, Resonant creation of indirect excitons in diamond at the phonon-assisted absorption edge, Eur. Phys. Lett. **104**, 47012 (2013).

[30] J. Omachi, T. Suzuki, K. Kato, N. Naka, K. Yoshioka, and M. Kuwata-Gonokami, Observation of Excitonic N-Body Bound States: Polyexcitons in Diamond, Phys. Rev. Lett. **111**, 026402 (2013).

[31] D. W. Snoke, D. Braun, and M. Cardona, Carrier thermalization in Cu_2O: Phonon emission by excitons, Phys. Rev. B **44**, 2991 (1991).

[32] E. Hanamura and H. Haug, Condensation effects of excitons, Phys. Rep. **33**, 209 (1977).

[33] D. W. Snoke, W. W. Rühle, Y.-C. Lu, and E. Bauser, Evolution of a nonthermal electron energy distribution in GaAs, Phys. Rev. B **45**, 10979 (1992).

[34] See Supplemental Material at http://link.aps.org/supplemental/10.1103/PhysRevB.92.201202 for the internal thermalization and relaxation times.

[35] H. Morimoto, Y. Hazama, K. Tanaka, and N. Naka, Exciton lifetime and diffusion length in high-purity chemical-vapor-deposition diamond (unpublished).

[36] F. M. Steranka and J. P. Wolfe, Spatial expansion of electron-hole plasma in Si, Phys. Rev. B **34**, 1014 (1986).

[37] M. Kozak, F. Trojanek, and P. Maly, Hot-carrier transport in diamond controlled by femtosecond laser pulses, New J. Phys. **17**, 053027 (2015).

[38] M. E. Levinshtein, S. L. Rumyantsev, and M. Shur, *Handbook Series on Semiconductor Parameters*, Vol. 1 (World Scientific, Singapore, 1996).

[39] B. K. Ridley, *Quantum Processes in Semiconductors* (Oxford University Press, New York, 1993), Chap. 3.

[40] D. P. Trauernicht and J. P. Wolfe, Drift and diffusion of paraexcitons in Cu_2O: Deformation-potential scattering in the low-temperature regime, Phys. Rev. B **33**, 8506 (1986).

[41] M. Kozak, F. Trojanek, and P. Maly, Temperature and density dependence of exciton dynamics in IIa diamond: Experimental and theoretical study, Phys. Status Solidi A **211**, 2244 (2014).

[42] L. Gherardi, A. Pellacani, and C. Jacoboni, Velocity autocorrelation function and low-temperature mobility of electrons in silicon, Lett. Nuovo Cimento **14**, 225 (1975).

[43] M. A. Tamor and J. P. Wolfe, Drift and Diffusion of Free Excitons in Si, Phys. Rev. Lett. **44**, 1703 (1980).